

A High Order Bound Preserving Finite Difference Linear Scheme for Incompressible Flows

Guoliang Zhang¹ and Tao Xiong^{2,*}

¹ School of Mathematical Sciences, Xiamen University, Xiamen, Fujian 361005, P.R. China.

² School of Mathematical Sciences and Fujian Provincial Key Laboratory of Mathematical Modeling and High-Performance Scientific Computing, Xiamen University, Xiamen, Fujian 361005, P.R. China.

Received 13 December 2021; Accepted (in revised version) 18 April 2022

Abstract. We propose a high order finite difference linear scheme combined with a high order bound preserving maximum-principle-preserving (MPP) flux limiter to solve the incompressible flow system. For such problem with highly oscillatory structure but not strong shocks, our approach seems to be less dissipative and much less costly than a WENO type scheme, and has high resolution due to a Hermite reconstruction. Spurious numerical oscillations can be controlled by the weak MPP flux limiter. Numerical tests are performed for the Vlasov-Poisson system, the 2D guiding-center model and the incompressible Euler system. The comparison between the linear and WENO type schemes, with and without the MPP flux limiter, will demonstrate the good performance of our proposed approach.

AMS subject classifications: 65M06, 65M20, 35M13

Key words: Finite difference scheme, high order Hermite reconstruction, MPP flux limiter, incompressible flow, Vlasov-Poisson.

1 Introduction

In this paper, we are interested in the numerical approximation of incompressible transport equations as

$$\begin{cases} \frac{\partial \rho}{\partial t} + \mathbf{U} \cdot \nabla \rho = 0, \\ \operatorname{div} \mathbf{U} = 0, \end{cases} \quad (1.1)$$

*Corresponding author. *Email addresses:* zglmth@stu.xmu.edu.cn (G. Zhang), txiong@xmu.edu.cn (T. Xiong)

where \mathbf{U} represents the advection field and ρ is a nonnegative density.

A typical example of application is the well known Vlasov-Poisson (VP) system arising in collisionless plasma physics. It describes the time evolution of particles under the effects of self-consistent electrostatic field and reads

$$\frac{\partial f}{\partial t} + \mathbf{v} \cdot \nabla_{\mathbf{x}} f + \mathbf{E} \cdot \nabla_{\mathbf{v}} f = 0, \quad (1.2)$$

$f := f(t, \mathbf{x}, \mathbf{v})$ is the distribution function in the phase space $(\mathbf{x}, \mathbf{v}) \in \mathbb{R}^d \times \mathbb{R}^d, d = 1, 2, 3$. $\mathbf{E} := \mathbf{E}(t, \mathbf{x})$ is the electric field, which can be determined by the Poisson's equation from an electric potential function $\Phi(t, \mathbf{x})$

$$\mathbf{E}(t, \mathbf{x}) = -\nabla_{\mathbf{x}} \Phi(t, \mathbf{x}), \quad -\Delta_{\mathbf{x}} \Phi(t, \mathbf{x}) = \rho(t, \mathbf{x}). \quad (1.3)$$

The charge density $\rho(t, \mathbf{x})$ is defined as

$$\rho(t, \mathbf{x}) = \int_{\mathbb{R}^d} f(t, \mathbf{x}, \mathbf{v}) d\mathbf{v}.$$

Another example is the two dimensional guiding-center model, which describes the evolution of the charge density ρ in a highly magnetized plasma in the transverse plane of a tokamak, is given by

$$\begin{cases} \frac{\partial \rho}{\partial t} + \mathbf{U} \cdot \nabla \rho = 0, \\ -\Delta \Phi = \rho, \end{cases} \quad (1.4)$$

where $\mathbf{U} = (-\Phi_y, \Phi_x)$ is a divergence free velocity. The two dimensional guiding center model can also be referred as an asymptotic model of the VP system by averaging in the velocity phase space, for details, see [28]. We notice that the guiding-center model (1.4) is in the same form as the two dimensional incompressible Euler equations in the vorticity stream function formulation, which describes the evolution of vortices in fluid hydrodynamics.

For the models mentioned above, they all have a transport equation coupled with a Poisson's equation for the advection velocity, and moreover, the advection velocity is divergence free. In the following, we refer them as incompressible flow models.

Many numerical schemes have been proposed for solving these models, especially recently, high order schemes are very attractive due to their high resolutions for such problems with rich solution structures. For example, deterministic methods, there are finite difference, finite volume and finite element Eulerian methods [10, 12, 18–20, 43, 51, 53, 54, 56, 59], semi-Lagrangian methods [4, 5, 7, 8, 13, 14, 23, 31–35, 38, 45, 46, 52, 58], and discontinuous Galerkin finite element methods [3, 6, 11, 15, 22, 24, 29, 55, 60], also see many other references therein. However, due to the highly oscillatory structure of such problems, linear type schemes for these problems would show significant spurious numerical oscillations, which might get worse with increased orders. Weighted essentially nonoscillatory (WENO) reconstruction, which was originally developed in the presence of both shocks

and small fine structures for fluid hydrodynamics of hyperbolic conservation laws, see for example [36], is frequently adopted in most of the finite difference and finite volume Eulerian or semi-Lagrangian methods mentioned above. For WENO type schemes, we can often observe the good performance of the WENO reconstruction on suppressing spurious oscillations [32, 43, 45, 51, 56], which can also be seen from our examples in the numerical section. However, for incompressible flow problems, their solutions are highly oscillatory but without strong discontinuities. We might expect excessive usage of the WENO reconstruction, which is computationally more expensive than a pure linear type scheme and too dissipative for certain classes of problems [25], especially for high dimensional problems with long time simulations. Although hybrid approaches of coupling a linear scheme and a WENO scheme can save some cost from the WENO reconstruction, for example the very recent work [16] and references therein, they still focus on problems with strong discontinuities and WENO may not be avoided.

In this paper, we propose to solve the incompressible flow problems with a high order linear scheme without WENO reconstruction. Linear schemes have the following several good properties: (1) less dissipative: for example, it preserves the L^2 norm (also energy and entropy for the VP system) better than the WENO type scheme; (2) less costly and easier implementation: without WENO reconstruction, it saves a lot of computational cost and can be easily implemented, especially when extended to high dimensional problems; (3) higher resolution if with a Hermite reconstruction. We adopt the scheme in [51] but with a Hermite linear reconstruction. In order to control the spurious numerical oscillations due to a linear type scheme, we seek to combine it with a newly developed high order bound preserving maximum-principle-preserving (MPP) flux limiter. The MPP flux limiter was first proposed by Xu et al. [26, 49], and then improved by Xiong et al. [43, 45]. It can be seen as a very weak limiter, which just pulls the numerical overshootings and undershootings back to its physical range, without excessive dissipating the solution within the range. Moreover, there is no further time step restriction on this MPP flux limiter from the original scheme for linear stabilities. We refer to [50] for a review of recent works on this bound preserving high order flux limiter. MPP or PP preserving schemes have also been developed for diffusion type problems, e.g., we refer to some recent works [17, 27, 39, 40, 48] and references therein. The coupling of the linear scheme and the MPP flux limiter keeps the original high order accuracy while maintaining a large CFL number. Due to the highly oscillatory but non discontinuous solutions of incompressible flow problems, the MPP flux limiter can serve as a necessary auxiliary tool for the linear scheme. The extra work from applying the MPP flux limiter at each final stage of a multi-stage Runge-Kutta time discretization, is much less than the WENO reconstruction. Numerical experiments, especially the bump-on-tail instability of long time simulation and the Kelvin-Helmholtz instability of the 2D guiding-center model are as benchmark tests, will be performed to demonstrate the good performance of our proposed approach.

The rest of the paper is organized as follows. In Section 2, we will describe the conservative finite difference schemes with both linear and WENO reconstructions, for the

completeness of comparison in the numerical section. The bound preserving MPP flux limiter will also be briefly reviewed. In Section 3, numerical experiments including the VP system, the Kelvin-Helmholtz instability of the 2D guiding center model and the incompressible Euler system will be studied. Conclusions are made in Section 4.

2 Finite difference scheme with Hermite reconstruction

In this section, we will describe our scheme to solve the VP system (1.2)-(1.3), the 2D guiding-center model (1.4) as well as the incompressible Euler system. Here we just consider $d = 1$ for the VP system. In common we will have a 2D transport equation with a divergence free velocity, coupled with a Poisson's type equation, which is one-dimensional (1D) for the VP system, and two-dimensional (2D) for the other two. In the following, we will take the 2D guiding-center model (1.4) as an example to describe our schemes. The other two models can be applied similarly.

We propose a finite difference scheme with a Hermite linear reconstruction for solving the 2D conservative transport equation. We adopt the scheme developed by Filbet and Yang [51], which has a Hermite WENO reconstruction. In the following, we will briefly recall the 2D conservative finite difference scheme and describe both the Hermite linear and WENO reconstructions. We note that the smooth indicators for the Hermite WENO reconstruction are modified as compared to [51]. The Poisson's equation for the electric potential function Φ will be solved by fast Fourier transform (FFT) for periodic boundary condition on an interval in one-dimension (1D) or periodic boundary conditions on a rectangular domain in two-dimension (2D), which will be omitted here. We refer to [51] for more details.

2.1 Conservative finite difference scheme

We consider the 2D transport equation in a conservative form

$$\partial_t \rho + \operatorname{div}_{\mathbf{x}}(\mathbf{U}\rho) = 0,$$

with $\mathbf{U} = \mathbf{U}(t, \mathbf{x})$ such that $\operatorname{div}_{\mathbf{x}}\mathbf{U} = 0$ and $\mathbf{x} = (x, y)$. For simplicity, we assume a uniform discretization of the computational domain $[x_{\min}, x_{\max}] \times [y_{\min}, y_{\max}]$ with $N_x \times N_y$ grid points

$$\begin{aligned} x_{\min} &= x_0 < x_1 < \cdots < x_{N_x-1} < x_{N_x} = x_{\max}, \\ y_{\min} &= y_0 < y_1 < \cdots < y_{N_y-1} < y_{N_y} = y_{\max}, \end{aligned}$$

where the mesh sizes are $\Delta x = x_{i+1} - x_i$ and $\Delta y = y_{j+1} - y_j$ for $0 \leq i \leq N_x, 0 \leq j \leq N_y$. A conservative finite difference scheme with Euler forward time discretization is defined as follows:

$$\rho_{i,j}^{n+1} = \rho_{i,j}^n - \Delta t \left(\frac{\hat{H}_{i+\frac{1}{2},j} - \hat{H}_{i-\frac{1}{2},j}}{\Delta x} + \frac{\hat{G}_{i,j+\frac{1}{2}} - \hat{G}_{i,j-\frac{1}{2}}}{\Delta y} \right), \quad (2.1)$$

where the time step is $\Delta t = t^{n+1} - t^n$. ρ_{ij}^n is the numerical value at time level t^n on the grid point (x_i, y_j) . $\hat{H}_{i+\frac{1}{2},j}$, $\hat{G}_{i,j+\frac{1}{2}}$ are the numerical fluxes in the x and y directions respectively.

2.2 Hermite linear reconstruction

For a finite difference scheme (2.1), the numerical fluxes $\hat{H}_{i+\frac{1}{2},j}$ and $\hat{G}_{i,j+\frac{1}{2}}$ are reconstructed dimension by dimension. Here we will take a 1D transport equation to illustrate on how to obtain a flux by a Hermite linear reconstruction. $\hat{H}_{i+\frac{1}{2},j}$ and $\hat{G}_{i,j+\frac{1}{2}}$ are obtained in this way along each of its own direction. The Hermite linear reconstruction is what we propose in this paper. A corresponding Hermite WENO reconstruction will be described in the next subsection, which is used for comparison in the numerical section.

Let us consider a prototype 1D conservative transport equation

$$\partial_t \rho + \partial_x (U\rho) = 0, \quad (2.2)$$

with velocity $U = U(t, x)$ and a uniform discretization with mesh size $\Delta x = x_{k+1} - x_k$ for $0 \leq k < N_x$. A conservative finite difference scheme for (2.2) can be written as

$$\rho_i^{n+1} = \rho_i^n - \frac{\Delta t}{\Delta x} (\hat{h}_{i+\frac{1}{2}} - \hat{h}_{i-\frac{1}{2}}),$$

where ρ_i^n is the numerical point value at time level t^n on the grid point x_i . $\hat{h}_{i+\frac{1}{2}}$ can be chosen as an upwind numerical flux, which is

$$\hat{h}_{i+\frac{1}{2}} = \begin{cases} h_{i+\frac{1}{2}}^-, & \text{if } \frac{U_i^n + U_{i+1}^n}{2} > 0, \\ h_{i+\frac{1}{2}}^+, & \text{otherwise.} \end{cases}$$

$h_{i+\frac{1}{2}}^\pm$ are fluxes reconstructed from $\{h_i^n = U_i^n \rho_i^n\}_i$ by a Hermite linear reconstruction, from the left and right sides of $x_{i+\frac{1}{2}}$ respectively, where U_i^n is the numerical velocity approximating $U(t^n, x_i)$. For simplicity, we drop the superscript n for h_i^n and $h_{i+\frac{1}{2}}^-$ is simply reconstructed by

$$h_{i+\frac{1}{2}}^- = \frac{1}{27} (-8h_{i-1} + 19h_i + 19h_{i+1} + 3G'_{i-3/2} - 6G'_{i+3/2}), \quad (2.3)$$

where the derivative of the primitive function $G'_{i+\frac{1}{2}}$ is given by a 6th order central difference approximation

$$G'_{i+\frac{1}{2}} = \frac{1}{60} [(h_{i+3} - h_{i-2}) - 8(h_{i+2} - h_{i-1}) + 37(h_{i+1} - h_i)], \quad (2.4)$$

$h_{i+\frac{1}{2}}^+$ can be obtained in mirror symmetric with respect to $x_{i+\frac{1}{2}}$.

2.3 Hermite WENO reconstruction

Now we will describe a fifth order Hermite WENO reconstruction to compute $h_{i+\frac{1}{2}}^-$ corresponding to (2.3). The procedure is outlined as follows. $h_{i+\frac{1}{2}}^+$ can also be obtained in mirror symmetric with respect to $x_{i+\frac{1}{2}}$. We drop the superscript n for h_i^n and we have

$$h_{i+\frac{1}{2}}^- = \omega_l h_l(x_{i+\frac{1}{2}}) + \omega_c h_c(x_{i+\frac{1}{2}}) + \omega_r h_r(x_{i+\frac{1}{2}}). \quad (2.5)$$

The three polynomials $h_l(x)$, $h_c(x)$ and $h_r(x)$ evaluating at $x_{i+\frac{1}{2}}$ are

$$\begin{cases} h_l(x_{i+\frac{1}{2}}) = -2h_{i-1} + 2h_i + G'_{i-\frac{3}{2}}, \\ h_c(x_{i+\frac{1}{2}}) = \frac{-h_{i-1} + 5h_i + 2h_{i+1}}{6}, \\ h_r(x_{i+\frac{1}{2}}) = \frac{h_i + 5h_{i+1} - 2G'_{i+\frac{3}{2}}}{4}, \end{cases}$$

where the weights ω_l , ω_c and ω_r are the nonlinear WENO weights and determined according to the smoothness indicators

$$\omega_k = \frac{\alpha_k}{\alpha_l + \alpha_c + \alpha_r}, \quad \alpha_k = \frac{c_k}{(\epsilon + \beta_k)^2}, \quad k = l, c, r.$$

In order to match (2.3), the linear coefficients are $c_l = 1/9$ and $c_c = c_r = 4/9$. The small parameter $\epsilon = 10^{-6}$ is to avoid the denominator to be 0.

To evaluate the smooth indicators β_l , β_c and β_r , we measure them on the cell $[x_{i-\frac{1}{2}}, x_{i+\frac{1}{2}}]$ instead of $[x_i, x_{i+1}]$ as in [51]. In this way, the smooth indicators are symmetric with respect to x_i , as we can see below:

$$\begin{aligned} \beta_l &= \int_{x_{i-\frac{1}{2}}}^{x_{i+\frac{1}{2}}} \Delta x (h'_l(x))^2 + \Delta x^3 (h''_l(x))^2 dx \\ &= \frac{13}{16} s_1^2 + \frac{3}{16} (s_1 - 4s_2)^2, \quad \text{with } s_1 = h_{i-1} - h_i, \quad s_2 = -3h_{i-1} + h_i + G'_{i-\frac{3}{2}}, \\ \beta_c &= \int_{x_{i-\frac{1}{2}}}^{x_{i+\frac{1}{2}}} \Delta x (h'_c(x))^2 + \Delta x^3 (h''_c(x))^2 dx \\ &= \frac{1}{4} s_1^2 + \frac{13}{12} s_2^2, \quad \text{with } s_1 = h_{i+1} - h_{i-1}, \quad s_2 = h_{i+1} - 2h_i + h_{i-1}, \\ \beta_r &= \int_{x_{i-\frac{1}{2}}}^{x_{i+\frac{1}{2}}} \Delta x (h'_r(x))^2 + \Delta x^3 (h''_r(x))^2 dx \\ &= \frac{13}{16} s_1^2 + \frac{3}{16} (s_1 - 4s_2)^2, \quad \text{with } s_1 = h_{i+1} - h_i, \quad s_2 = -3h_{i+1} + h_i + G'_{i+\frac{3}{2}}. \end{aligned}$$

2.4 High order Runge-Kutta time discretization

The first order Euler forward time discretization (2.1) can be generalized to high order Runge-Kutta (RK) time discretization [37]. For example, if we write (2.1) in the following form

$$\rho^{n+1} = \rho^n + \Delta t L(\rho^n),$$

here the subscripts for ρ are dropped and the operator L denotes the spatial discretization, then a 4th order RK time discretization can be written as

$$\begin{cases} \rho^{(1)} = \rho^n + \frac{1}{2} \Delta t L(\rho^n), \\ \rho^{(2)} = \rho^n + \frac{1}{2} \Delta t L(\rho^{(1)}), \\ \rho^{(3)} = \rho^n + \Delta t L(\rho^{(2)}), \\ \rho^{n+1} = \rho^n + \frac{1}{6} \Delta t \left(L(\rho^n) + 2L(\rho^{(1)}) + 2L(\rho^{(2)}) + L(\rho^{(3)}) \right), \end{cases} \quad (2.6)$$

with a CFL number $\frac{2}{3}$ for linear stability [37]. The last stage of (2.6) can be written in the same form as (2.1), which is

$$\rho_{i,j}^{n+1} = \rho_{i,j}^n - \Delta t \left(\frac{\hat{H}_{i+\frac{1}{2},j}^{rk} - \hat{H}_{i-\frac{1}{2},j}^{rk}}{\Delta x} + \frac{\hat{G}_{i,j+\frac{1}{2}}^{rk} - \hat{G}_{i,j-\frac{1}{2}}^{rk}}{\Delta y} \right), \quad (2.7)$$

where the numerical flux $\hat{H}_{i+\frac{1}{2},j}^{rk}$ is accumulated from all formal stages, that is

$$\hat{H}^{rk} = \frac{1}{6} \left(\hat{H}^{(0)} + 2\hat{H}^{(1)} + 2\hat{H}^{(2)} + \hat{H}^{(3)} \right),$$

where $\hat{H}^{(l)}$ is the numerical flux at the corresponding l -th stage, and the subscript $(i+\frac{1}{2},j)$ is dropped for clarity. $\hat{G}_{i,j+\frac{1}{2}}^{rk}$ is defined similarly.

2.5 Bound preserving MPP flux limiter

For a high order bound preserving limiter, we adopt the parametrized maximum-principle-preserving (MPP) flux limiter developed in [43, 45]. The MPP flux limiter is only applied at the final stage of (2.6), that is (2.7). Due to the same form of (2.1) and (2.7), the MPP flux limiter is defined as a convex combination of a first order monotone flux and the high order flux in (2.7). In the following, we first describe a first order monotone MPP scheme for a general incompressible flow system, then we recall a specific first order monotone MPP scheme developed in [43] for the incompressible flow system with the Poisson's equation.

For a general incompressible flow system with divergence free condition

$$\begin{cases} \partial_t \rho + \operatorname{div}_{\mathbf{x}}(\mathbf{U}\rho) = 0, \\ \operatorname{div}_{\mathbf{x}} \mathbf{U} = 0, \end{cases} \quad (2.8)$$

a first order scheme can be defined as

$$\begin{cases} \rho_{i,j}^{n+1} = \rho_{i,j}^n - \lambda_x \left(U_{i+\frac{1}{2},j}^- \rho_{i,j}^n + U_{i+\frac{1}{2},j}^+ \rho_{i+1,j}^n - U_{i-\frac{1}{2},j}^- \rho_{i-1,j}^n - U_{i-\frac{1}{2},j}^+ \rho_{i,j}^n \right) \\ \quad - \lambda_y \left(U_{i,j+\frac{1}{2}}^- \rho_{i,j}^n + U_{i,j+\frac{1}{2}}^+ \rho_{i,j+1}^n - U_{i,j-\frac{1}{2}}^- \rho_{i,j-1}^n - U_{i,j-\frac{1}{2}}^+ \rho_{i,j}^n \right), \\ \frac{1}{\Delta x} \left(U_{i+\frac{1}{2},j}^- + U_{i+\frac{1}{2},j}^+ - U_{i-\frac{1}{2},j}^- + U_{i-\frac{1}{2},j}^+ \right) + \frac{1}{\Delta y} \left(U_{i,j+\frac{1}{2}}^- + U_{i,j+\frac{1}{2}}^+ - U_{i,j-\frac{1}{2}}^- - U_{i,j-\frac{1}{2}}^+ \right) = 0, \end{cases} \quad (2.9)$$

where $\lambda_x = \Delta t / \Delta x$ and $\lambda_y = \Delta t / \Delta y$. If the scheme (2.9) is a consistent discretization to (2.8), we have the following statement:

Proposition 2.1. For a first order consistent scheme (2.9) solving the incompressible system (2.8), it is monotone and MPP, if the time step is small enough, e.g.,

$$\Delta t \leq \frac{1}{2 \max |\mathbf{U}|} \frac{\Delta x \Delta y}{\Delta x + \Delta y} \quad (2.10)$$

and the coefficients have signs that

$$U_{i+\frac{1}{2},j}^- \geq 0, \quad U_{i+\frac{1}{2},j}^+ < 0, \quad U_{i,j+\frac{1}{2}}^- \geq 0, \quad U_{i,j+\frac{1}{2}}^+ < 0, \quad (2.11)$$

for all i, j .

Proof. We can rewrite the first equation in the scheme (2.9) to be

$$\rho_{i,j}^{n+1} = \alpha_{i,j} \rho_{i,j}^n + \alpha_{i+1,j} \rho_{i+1,j}^n + \alpha_{i-1,j} \rho_{i-1,j}^n + \alpha_{i,j+1} \rho_{i,j+1}^n + \alpha_{i,j-1} \rho_{i,j-1}^n, \quad (2.12)$$

with

$$\begin{cases} \alpha_{i,j} = 1 - \lambda_x \left(U_{i+\frac{1}{2},j}^- - U_{i-\frac{1}{2},j}^+ \right) - \lambda_y \left(U_{i,j+\frac{1}{2}}^- - U_{i,j-\frac{1}{2}}^+ \right), \\ \alpha_{i+1,j} = -\lambda_x U_{i+\frac{1}{2},j}^+, \quad \alpha_{i-1,j} = \lambda_x U_{i-\frac{1}{2},j}^-, \\ \alpha_{i,j+1} = -\lambda_y U_{i,j+\frac{1}{2}}^+, \quad \alpha_{i,j-1} = \lambda_y U_{i,j-\frac{1}{2}}^-. \end{cases}$$

It is easy to check that $\alpha_{i,j}, \alpha_{i\pm 1,j}, \alpha_{i,j\pm 1}$ are all positive if the two conditions (2.10) and (2.11) are satisfied. Moreover,

$$\alpha_{i,j} + \alpha_{i+1,j} + \alpha_{i-1,j} + \alpha_{i,j+1} + \alpha_{i,j-1} = 1,$$

due to the enforced discrete divergence free condition in (2.9). Since (2.12) is a convex combination, so it is monotone and MPP. \square

A specific first order monotone MPP scheme depends on how to choose $U_{i+\frac{1}{2},j}^\pm$ and $U_{i,j+\frac{1}{2}}^\pm$. By using a potential function Φ , where $\mathbf{U} = (-\Phi_y, \Phi_x)$, a first order monotone MPP scheme with Lax-Friedrichs flux defined in [43] is to take:

$$\begin{cases} U_{i+\frac{1}{2},j}^- = \frac{1}{2} \left(\alpha_x - \frac{\Phi_{i,j+1} - \Phi_{i,j}}{\Delta y} \right), & U_{i+\frac{1}{2},j}^+ = \frac{1}{2} \left(-\alpha_x - \frac{\Phi_{i+1,j} - \Phi_{i+1,j-1}}{\Delta y} \right), \\ U_{i,j+\frac{1}{2}}^- = \frac{1}{2} \left(\alpha_y + \frac{\Phi_{i+1,j} - \Phi_{i,j}}{\Delta x} \right), & U_{i,j+\frac{1}{2}}^+ = \frac{1}{2} \left(-\alpha_y + \frac{\Phi_{i,j+1} - \Phi_{i-1,j+1}}{\Delta x} \right), \end{cases} \quad (2.13)$$

where

$$\alpha_x = \max_{i,j} \left| \frac{\Phi_{i,j+1} - \Phi_{i,j}}{\Delta y} \right|, \quad \alpha_y = \max_{i,j} \left| \frac{\Phi_{i+1,j} - \Phi_{i,j}}{\Delta x} \right|.$$

In this paper, the potential function Φ is obtained by solving the Poisson's equation $-\Delta\Phi = \rho$ with FFT.

Now to describe the MPP flux limiter, we write the first order monotone MPP scheme in a conservative flux difference form

$$\rho_{i,j}^{n+1} = \rho_{i,j}^n - \lambda_x \left(\hat{h}_{i+\frac{1}{2},j} - \hat{h}_{i-\frac{1}{2},j} \right) - \lambda_y \left(\hat{g}_{i,j+\frac{1}{2}} - \hat{g}_{i,j-\frac{1}{2}} \right), \quad (2.14)$$

with

$$\begin{cases} \hat{h}_{i+\frac{1}{2},j} = \frac{1}{2} \left(\alpha_x - \frac{\Phi_{i,j+1} - \Phi_{i,j}}{\Delta y} \right) \rho_{i,j}^n + \frac{1}{2} \left(-\alpha_x - \frac{\Phi_{i+1,j} - \Phi_{i+1,j-1}}{2\Delta y} \right) \rho_{i+1,j}^n, \\ \hat{g}_{i,j+\frac{1}{2}} = \frac{1}{2} \left(\alpha_y + \frac{\Phi_{i+1,j} - \Phi_{i,j}}{\Delta x} \right) \rho_{i,j}^n + \frac{1}{2} \left(-\alpha_y + \frac{\Phi_{i,j+1} - \Phi_{i-1,j+1}}{\Delta x} \right) \rho_{i,j+1}^n. \end{cases} \quad (2.15)$$

$\hat{h}_{i+\frac{1}{2},j}$ and $\hat{g}_{i,j+\frac{1}{2}}$ are first order monotone numerical fluxes. Similarly, (2.7) is

$$\rho_{i,j}^{n+1} = \rho_{i,j}^n - \lambda_x \left(\hat{H}_{i+1/2,j}^{rk} - \hat{H}_{i-1/2,j}^{rk} \right) - \lambda_y \left(\hat{G}_{i,j+1/2}^{rk} - \hat{G}_{i,j-1/2}^{rk} \right). \quad (2.16)$$

In order to ensure maximum principle, we are looking for type of limiters

$$\begin{cases} \tilde{H}_{i+1/2,j} = \theta_{i+1/2,j} (\hat{H}_{i+1/2,j}^{rk} - \hat{h}_{i+1/2,j}) + \hat{h}_{i+1/2,j}, \\ \tilde{G}_{i,j+1/2} = \theta_{i,j+1/2} (\hat{G}_{i,j+1/2}^{rk} - \hat{g}_{i,j+1/2}) + \hat{g}_{i,j+1/2}, \end{cases} \quad (2.17)$$

such that

$$\rho_m \leq \rho_{i,j}^n - \lambda_x (\tilde{H}_{i+1/2,j} - \tilde{H}_{i-1/2,j}) - \lambda_y (\tilde{G}_{i,j+1/2} - \tilde{G}_{i,j-1/2}) \leq \rho_M. \quad (2.18)$$

(2.17) and (2.18) form coupled inequalities for the limiting parameters $\theta_{i+1/2,j}, \theta_{i,j+1/2}$. We will need to find a group of numbers $\Lambda_{L,i,j}, \Lambda_{R,i,j}, \Lambda_{D,i,j}, \Lambda_{U,i,j}$, such that (2.18) is satisfied with

$$(\theta_{i-1/2,j}, \theta_{i+1/2,j}, \theta_{i,j-1/2}, \theta_{i,j+1/2}) \in [0, \Lambda_{L,i,j}] \times [0, \Lambda_{R,i,j}] \times [0, \Lambda_{D,i,j}] \times [0, \Lambda_{U,i,j}].$$

This is achieved in a decoupled way for the minimum and maximum parts. For the maximum value case, we let

$$\Gamma_{i,j} = \rho_M - \left(\rho_{i,j} - \lambda_x (\hat{h}_{i+1/2,j} - \hat{h}_{i-1/2,j}) - \lambda_y (\hat{g}_{i,j+1/2} - \hat{g}_{i,j-1/2}) \right) \geq 0, \quad (2.19)$$

and denote

$$\begin{cases} F_{i-1/2,j} = +\lambda_x \left(\hat{H}_{i-1/2,j}^{rk} - \hat{h}_{i-1/2,j} \right), \\ F_{i+1/2,j} = -\lambda_x \left(\hat{H}_{i+1/2,j}^{rk} - \hat{h}_{i+1/2,j} \right), \\ F_{i,j-1/2} = +\lambda_y \left(\hat{G}_{i,j-1/2}^{rk} - \hat{g}_{i,j-1/2} \right), \\ F_{i,j+1/2} = -\lambda_y \left(\hat{G}_{i,j+1/2}^{rk} - \hat{g}_{i,j+1/2} \right), \end{cases} \quad (2.20)$$

then (2.18) can be rewritten as

$$\theta_{i+1/2,j}F_{i+1/2,j} + \theta_{i-1/2,j}F_{i-1/2,j} + \theta_{i,j+1/2}F_{i,j+1/2} + \theta_{i,j-1/2}F_{i,j-1/2} \leq \Gamma_{i,j}. \quad (2.21)$$

We shall now focus on decoupling the inequalities (2.21): for the single node (i, j) ,

1. Identify positive values out of the four locally defined numbers $F_{i-1/2,j}$, $F_{i+1/2,j}$, $F_{i,j-1/2}$, $F_{i,j+1/2}$;
2. Corresponding to those positive values, collectively, the limiting parameters can be defined. For example, if $F_{i+1/2,j}, F_{i-1/2,j} > 0$ and $F_{i,j-1/2}, F_{i,j+1/2} \leq 0$, then

$$\begin{cases} \Lambda_{i+1/2,j}^M = \Lambda_{i-1/2,j}^M = \min\left(\frac{\Gamma_{i,j}}{F_{i+1/2,j} + F_{i-1/2,j}}, 1\right), \\ \Lambda_{i,j-1/2}^M = \Lambda_{i,j+1/2}^M = 1, \end{cases} \quad (2.22)$$

that is, all high order fluxes which possibly contribute (beyond that of the first order fluxes, which is not good) to the overshooting or undershooting of the updated value shall be limited by the same scaling. Similarly we can find $\Lambda_{i,j\pm 1/2}^M$ and also similarly for the minimum value case of $\Lambda_{i\pm 1/2,j}^m$ and $\Lambda_{i,j\pm 1/2}^m$. Therefore the range of the limiting parameters satisfying MPP for a single node (i, j) is defined by

$$\begin{cases} \Lambda_{L,i,j} = \min(\Lambda_{i-1/2,j}^M, \Lambda_{i-1/2,j}^m), \\ \Lambda_{R,i,j} = \min(\Lambda_{i+1/2,j}^M, \Lambda_{i+1/2,j}^m), \\ \Lambda_{U,i,j} = \min(\Lambda_{i,j+1/2}^M, \Lambda_{i,j+1/2}^m), \\ \Lambda_{D,i,j} = \min(\Lambda_{i,j-1/2}^M, \Lambda_{i,j-1/2}^m). \end{cases} \quad (2.23)$$

Considering the limiters from neighboring nodes, finally we let

$$\begin{cases} \theta_{i+1/2,j} = \min(\Lambda_{R,i,j}, \Lambda_{L,i+1,j}), \\ \theta_{i,j+1/2} = \min(\Lambda_{U,i,j}, \Lambda_{D,i,j+1}). \end{cases} \quad (2.24)$$

Substituting (2.24) into (2.17), our final scheme is (2.16) by replacing the fluxes from (2.17).

2.6 Boundary treatment

For the above discussions, the periodic or compact support boundary condition is assumed. However, the MPP flux limiter can also be applied to other types of boundary conditions, such as inflow-outflow or wall with reflective boundary conditions. For inflow-outflow or reflective boundary conditions, the values at the boundary or ghost points, are determined from the physical boundary condition, or from the values within the computational domain. They are not updated by the numerical scheme itself. In

the MPP limiter, we do not need to take into account these values. Namely in (2.24), on the left boundary, we take $\theta_{1/2,j} = \Lambda_{L,1,j}$ while on the right boundary, we take $\theta_{N-1/2,j} = \Lambda_{R,N-1,j}$, where $\Lambda_{L,1,j}$ and $\Lambda_{R,N-1,j}$ are within the computational domain. Similarly along the y direction. This has already been used in [44] to show its effectiveness.

In the following, we will take a 1D linear transport problem as an example, to briefly discuss how to impose MPP-satisfied time-dependent inflow-outflow boundary conditions, which will be used to verify the performance of our proposed scheme. The problem is

$$\begin{cases} \rho_t + \rho_x = 0, \\ \rho(x,0) = \rho_0(x), \end{cases} \quad (2.25)$$

on the computational domain $[0,L]$ with an inflow boundary $u(0,t) = g(t)$ on the left which is time-dependent, and outflow on the right at $x = L$. Numerically with a high order Runge-Kutta time discretization, instead of precisely imposing the intermediate physical boundary conditions which reduces the order at the boundary, the following expressions for the intermediate boundary values at $x = 0$ are suggested. Taking the fourth order Runge-Kutta time discretization (2.6) as an example, from time level t^n to t^{n+1} , they are

$$\begin{cases} \rho_0^{(0)} = g(t^n), \\ \rho_0^{(1)} = g(t^n) + \frac{\Delta t}{2} g'(t^n), \\ \rho_0^{(2)} = g(t^n) + \frac{\Delta t}{2} g'(t^n) + \frac{\Delta t^2}{4} g''(t^n), \\ \rho_0^{(3)} = g(t^n) + \Delta t g'(t^n) + \frac{\Delta t^2}{2} g''(t^n) + \frac{\Delta t^3}{4} g'''(t^n), \end{cases} \quad (2.26)$$

where $\rho_0^{(\ell)}$ for $\ell = 0,1,2,3$ are the stage values of ρ at $x = 0$. For more details and other order Runge-Kutta schemes, we refer to [9]. In case of nonlinear problems $\rho_t + f(\rho)_x = 0$, see [1,30].

For a high order finite difference spatial discretization, we need to further assign boundary values at ghost points. For the linear problem (2.25), we adopt the inverse Lax-Wendroff method for the inflow boundary, as discussed in [41]. With a fifth order scheme, a fifth order Taylor approximation to the values at the ghost points are constructed, which are

$$\rho_j^{(\ell)} = \sum_{k=0}^4 \frac{(j\Delta x)^k}{k!} (\partial_x)^k \rho_0^{(\ell)}, \quad j = -1, -2, -3. \quad (2.27)$$

Here $(\partial_x)^k \rho_0^{(\ell)}$ is the k -th order partial derivative of $\rho(x,t)$ along x at $x = 0$ on the intermediate time stages, and $(\partial_x)^0 \rho_0^{(\ell)} = \rho_0^{(\ell)}$ which are given by (2.26). Using the inverse Lax-Wendroff method for the linear problem (2.25), we have $(\partial_x)^k \rho_0^{(\ell)} = (-1)^k (\partial_t)^k \rho_0^{(\ell)}$,

e.g., the first order derivatives when $k=1$ are given as

$$\begin{cases} \partial_x \rho_0^{(0)} = -g'(t^n), \\ \partial_x \rho_0^{(1)} = -g'(t^n) - \frac{\Delta t}{2} g''(t^n), \\ \partial_x \rho_0^{(2)} = -g'(t^n) - \frac{\Delta t}{2} g''(t^n) - \frac{\Delta t^2}{4} g'''(t^n), \\ \partial_x \rho_0^{(3)} = -g'(t^n) - \Delta t g''(t^n) - \frac{\Delta t^2}{2} g'''(t^n) - \frac{\Delta t^3}{4} g^{(4)}(t^n). \end{cases} \quad (2.28)$$

Similarly for higher order k 's. An efficient implementation for nonlinear problems can be referred to [42, 57]. For the outflow boundary, a high order extrapolation is used [41, 47].

We would mention that the inflow boundary treatment (2.27) may not necessarily preserve the MPP property, since they are only high order approximations to the exact boundary values. Numerically, a simple cut-off is taken to ensure these boundary values are within the physical bounds. Namely, sequentially we take

$$\rho_j^{(\ell),new} = \min(\rho_j^{(\ell)}, \rho_M), \quad \rho_j^{(\ell),new} = \max(\rho_j^{(\ell)}, \rho_m), \quad j = -1, -2, -3. \quad (2.29)$$

This will not affect the high order of the scheme. As if overshoots or undershoots exist in the approximations of smooth solutions, they are also high order approximations to the corresponding bounds. The cut-off is a high order modification. Similarly for the outflow boundary. The boundary treatments for 2D problems of finite difference schemes are done dimension by dimension, which are similar to the 1D case, we omit them to save space.

3 Numerical examples

In this section, we will apply the 5th order finite difference scheme with Hermite linear reconstruction (2.3) and (2.4), coupled with the bound preserving MPP flux limiter, which we denote as "HLinear5 MPP", to test its good performance. The Hermite linear scheme without bound preserving MPP flux limiter is denoted as "HLinear5", while those with Hermite WENO reconstruction (2.5) are denoted as "HWENO5 MPP" and "HWENO5" for with and without MPP flux limiter correspondingly. All the schemes without Hermite reconstruction, for example the one in [43], will be denoted as "WENO5 MPP" and "WENO5", and the corresponding linear schemes as "Linear5 MPP" and "Linear5", respectively. They will also be used for comparison in the following. The time step is taken as

$$\Delta t = \text{CFL} / (\alpha_x / \Delta x + \alpha_y / \Delta y),$$

where $\alpha_x = \|U_x\|_{L^\infty}$, $\alpha_y = \|U_y\|_{L^\infty}$ and we take the CFL number to be $\text{CFL} = 0.6$ in all the following tests.

We would emphasize that to apply the MPP limiter, the minimum and maximum values of the bounds are taken from the initial data, which can be explicitly determined for all the tests here.

3.1 Linear transport equations

Example 3.1. We take a 2D linear transport equation $\rho_t + \rho_x + \rho_y = 0$ with initial condition

$$\rho(0, x, y) = \sin^4(x) + \sin^4(y), \quad (3.1)$$

on the domain $[0, 2\pi]^2$ with periodic boundary conditions, to test the accuracy of the “HLinear5 MPP” and “HLinear5” schemes. The exact solution is

$$\rho(t, x, y) = \sin^4(x-t) + \sin^4(y-t). \quad (3.2)$$

The solution is within $[0, 2]$. From Table 1, we can clearly observe undershootings without the MPP limiter, while with limiter the lower bound is well preserved (as is for the upper bound) and 5th order accuracy is maintained. We would mention that for all other schemes we considered in this section, the accuracies are all tested and perform similarly. We omit them to save space.

Then we consider the 1D linear transport equation (2.25) with an inflow-outflow boundary condition. First we verify the inflow-outflow boundary treatment as described in Section 2.6, with or without the MPP limiter, can preserve the high order accuracy for smooth solutions. Here the initial condition is chosen to be

$$\rho(0, x) = \sin^4(x), \quad (3.3)$$

on the computational domain $[0, 2\pi]$. We take the exact solution to be $\rho(x, t) = \sin^4(x-t)$, and the corresponding inflow boundary is given as $g(t) = \sin^4(t)$. The “HLinear5 MPP” and “HLinear5” schemes are considered. In Table 2, we show the errors and orders for both schemes at the final time $T = \pi/2$. As we can see, fifth order is obtained for both schemes. For the solution without the MPP limiter, the minimum value of ρ becomes to be negative at the final time T . However, they become positive after using the MPP limiter. Besides, we mention that at the inflow boundary, when the solution is close to

Table 1: Accuracy test for the 2D linear transport equation in Example 3.1. ρ_{\min} is the minimum numerical solution. “WO” stands for “without limiter”, “WL” stands for “with limiter”. $T=1$.

	N	L^1 error	order	L^∞ error	order	ρ_{\min}
WO	32	5.00e-04	–	1.29e-03	–	-0.001019
	64	1.90e-05	4.72	4.91e-05	4.72	-4.244e-05
	128	6.41e-07	4.89	1.68e-06	4.87	-1.242e-06
	256	2.05e-08	4.97	5.35e-08	4.97	-4.403e-08
WL	32	5.16e-04	–	1.33e-03	–	0.0003958
	64	1.90e-05	4.77	5.54e-05	4.59	5.522e-06
	128	6.41e-07	4.89	2.07e-06	4.74	9.832e-13
	256	2.05e-08	4.97	7.78e-08	4.73	1.712e-09

Table 2: Accuracy test for the 1D linear transport equation (2.25) with an inflow-outflow boundary condition and initial condition (3.3). ρ_{\min} is the minimum numerical solution. "WO" stands for "without limiter", "WL" stands for "with limiter". $T = \pi/2$.

	N	L^1 error	order	L^∞ error	order	ρ_{\min}	$1 - \rho_{-1}$
WO	40	1.83e-04	–	4.30e-04	–	-3.289e-04	-5.545e-05
	80	6.86e-06	4.74	1.56e-05	4.78	-1.177e-05	-3.398e-06
	160	2.27e-07	4.92	4.82e-07	5.02	-3.838e-07	-2.218e-07
	320	7.21e-09	4.98	1.46e-08	5.05	-1.217e-08	-2.096e-08
WL	40	1.88e-04	–	4.33e-04	–	3.290e-05	N/A
	80	6.98e-06	4.75	2.57e-05	4.07	1.882e-07	N/A
	160	2.27e-07	4.94	9.48e-07	4.76	1.123e-09	N/A
	320	7.22e-09	4.98	3.11e-08	4.93	3.738e-11	N/A

the upper or lower bound, the numerical boundary value would exceed the bounds. E.g. at the ghost point $j = -1$, the value ρ_{-1} exceeds the upper bound 1 at one time step prior to T , which are shown in the last column of Table 2. These overshoots are not observed, denoted as "N/A" after applying cut-off for these boundary values, and the accuracy is not affected, which verify the effectiveness of our proposed approach.

Next we take another initial condition which is not periodic

$$\rho(0, x) = \sin(4x(x - 2\pi)). \quad (3.4)$$

The computational domain is $[0, 2\pi]$, with the inflow-outflow boundary condition $g(t) = \sin(4t(t + 2\pi))$. The exact solution is

$$\rho(t, x) = \sin(4(x - t)(x - t - 2\pi)), \quad (3.5)$$

which is a highly oscillatory solution. In Fig. 1, we show the results for both linear and WENO type schemes, without and with the MPP limiter respectively. Two ghost point values at both left and right boundaries are also included, corresponding to inflow and outflow boundary treatments. From the figures, we can observe that the "HLinear5" scheme has better resolution than the "Linear5" scheme, due to a Hermite reconstruction for such a highly oscillatory solutions, while linear schemes are much better than WENO type schemes due to less dissipation. We can also see the MPP limiter has very little affection on the solutions, but it can well control the solutions within the global physical range $[-1, 1]$. Besides, the simple cut-off can drag the ghost point values back into the physical range, without affecting the solutions within the computational domain. This example clearly demonstrates the good performance of "HLinear5 MPP", as compared to the other five schemes, especially WENO type schemes.

In the following, we will focus on the "HLinear5" and "HLinear5 MPP" schemes, and compare them to their corresponding WENO approaches, which are "HWENO5"

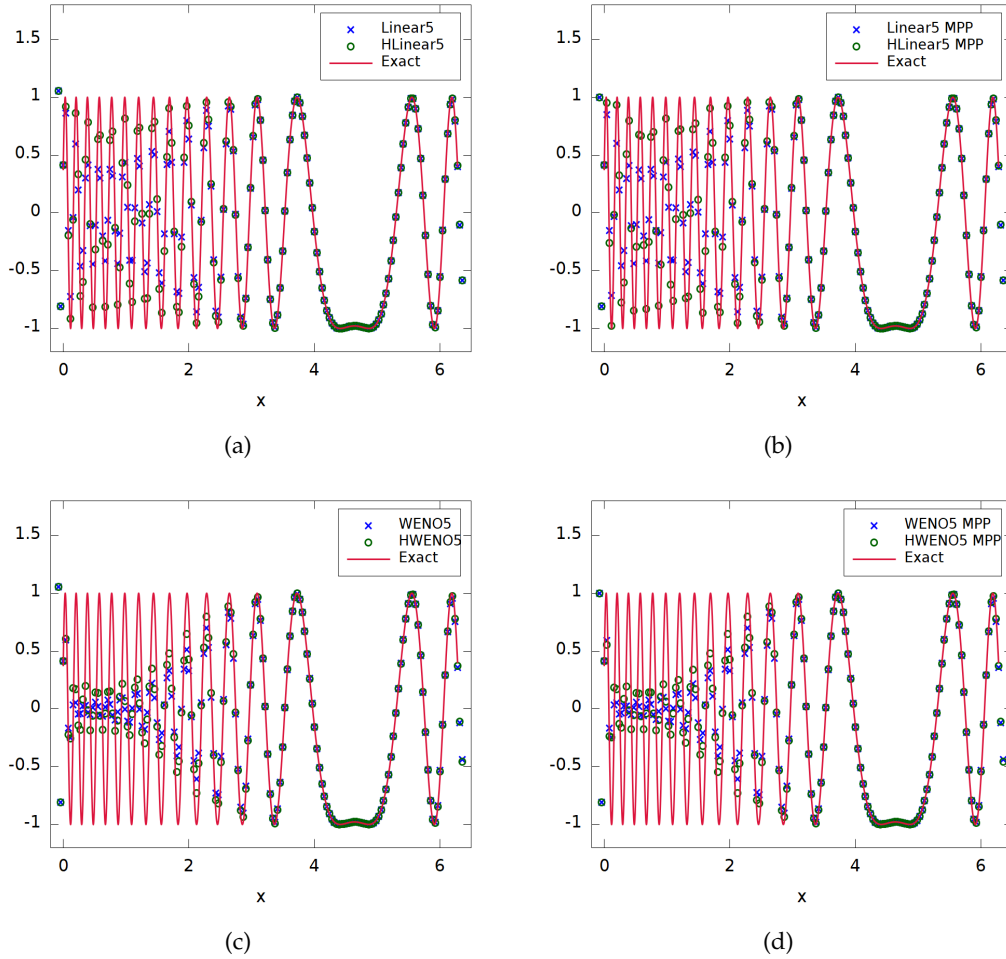


Figure 1: 1D linear equation (2.25) with the exact solution (3.5) at $T = 1.5$. Top: linear schemes; bottom: WENO schemes; left: without MPP limiter; right: with MPP limiter. $N = 160$.

and “HWENO5 MPP” respectively. We will further show “HLinear5 MPP” is a very good scheme for highly oscillatory solutions without discontinuities, which appear in the incompressible flows.

3.2 Vlasov-Poisson system

In this subsection, we consider the VP system (1.2) and (1.3) with 1D in x and 1D in v , and periodic boundary condition in both directions. We take $\mathbf{x} = (x, v)$ and use N_v instead of N_y for the special meaning of the argument v here. The cut-off domain in the v direction is taken to be $[-2\pi, 2\pi]$ if without specifications. The VP system preserves several norms, which should remain constant in time:

1. L^p norm, $1 \leq p < \infty$:

$$\|f\|_p = \left(\int_v \int_x |f(x,v,t)|^p dx dv \right)^{\frac{1}{p}}. \quad (3.6)$$

2. Energy:

$$\text{Energy} = \int_v \int_x f(x,v,t)v^2 dx dv + \int_x E^2(x,t) dx, \quad (3.7)$$

where $E(x,t)$ is the electric field.

3. Entropy:

$$\text{Entropy} = \int_v \int_x f(x,v,t) \log(f(x,v,t)) dx dv. \quad (3.8)$$

We will track the relative deviations of these quantities numerically to measure the quality of our numerical scheme. The relative deviation is defined to be the deviation away from the corresponding initial value divided by the magnitude of the initial value. The mass conservation over time $\int_v \int_x f(x,v,t) dx dv$ is obvious for conservative schemes, which is the same as the L^1 norm when f is positive, so only the L^1 norm is shown below. We would also note that for the VP system, although the minimum part is known as positivity preserving, however, due to a cut-off domain in the v direction, the minimum value might be close to but above 0. We clearly indicate the minimum and maximum values from the initial data for the tests below.

Example 3.2. (Accuracy test) We first consider the VP system with the following initial condition

$$f(0,x,v) = \frac{1}{\sqrt{2\pi}} \cos^4(kx) \exp\left(-\frac{v^2}{2}\right), \quad (3.9)$$

and periodic boundary conditions on the computational domain $[0,4\pi] \times [-4\pi,4\pi]$, where $k=0.5$, to test the accuracy of the schemes for this system. From the initial data, the solution should be within the range $[0, \frac{1}{\sqrt{2\pi}}]$.

In Table 3, we show the L^1 and L^∞ errors and orders for the ‘‘HLinear5’’ and ‘‘HLinear5 MPP’’ scheme respectively. For this example, 5th order accuracy can also be observed as mesh refinement. Without limiter, the solution of the distribution function does not preserve positivity, while with limiter, all values are above 0. Here we measure the errors on two consecutive mesh sizes by double refinement, since the exact solution is not explicitly available.

Example 3.3. (Strong Landau damping) We then consider the strong Landau damping with the initial condition:

$$f(0,x,v) = \frac{1}{\sqrt{2\pi}} (1 + \alpha \cos(kx)) \exp\left(-\frac{v^2}{2}\right), \quad (3.10)$$

Table 3: L^1 and L^∞ errors and orders for the VP system with initial condition (3.9) at $T=1$. “WL” denotes the scheme with limiters, “WO” denotes the scheme without limiters. “ f_{\min} ” is the minimum of the numerical solution. Mesh size $N_v=2N_x$.

	N_x	L^1 error	order	L^∞ error	order	f_{\min}
WO	64	1.66e-05	–	0.0004144	–	-1.317e-06
	128	6.83e-07	4.60	1.913e-05	4.44	-2.197e-08
	256	2.54e-08	4.75	7.137e-07	4.75	-1.777e-09
	512	8.29e-10	4.94	2.342e-08	4.93	-5.535e-11
WL	64	1.68e-05	–	0.0004177	–	1.59e-32
	128	6.85e-07	4.62	1.915e-05	4.45	1.768e-34
	256	2.54e-08	4.75	7.136e-07	4.75	2.339e-35
	512	8.30e-10	4.94	2.342e-08	4.93	4.797e-36

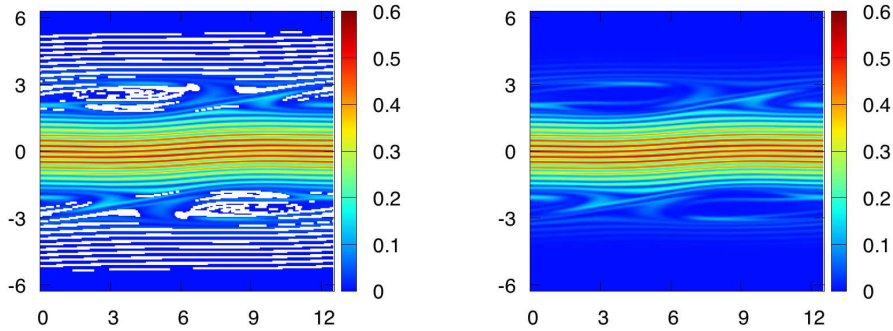


Figure 2: Strong Landau damping at $T=50$. Left: without limiter; Right: with limiter. Mesh grid: 256×256 .

where $\alpha = 0.5$ and $k = 0.5$. The length of the domain in the x-direction is $L = \frac{2\pi}{k}$, which is similar in the following two examples. For this problem, from the initial data, the solution should be within the range $[\frac{1}{\sqrt{2\pi}}(1-\alpha)\exp(-\frac{(2\pi)^2}{2}), \frac{1}{\sqrt{2\pi}}(1+\alpha)]$. In Fig. 2, we plot the surface of the distribution function f at $T=50$ in the range of $[0, 0.6]$. The mesh grid is 256×256 . We can observe that without limiter, the solution can be negative (white spots), while negative values are eliminated by the scheme with limiter, similarly for the following examples. Then in Fig. 3, we show the time evolution of the electric field in L^2 norm and L^∞ norm, the relative derivation of the discrete L^1 norm, L^2 norm, kinetic energy and entropy. From this figure, we can see that the electric field for all schemes are almost the same. The linear type scheme can preserve the L^2 norm and entropy better than the WENO type scheme, where the MPP limiter does not significantly affect these two quantities. However, for the L^1 norm and energy, the linear scheme without limiter performs much worse than the WENO type scheme, but after with limiter, it is the best.

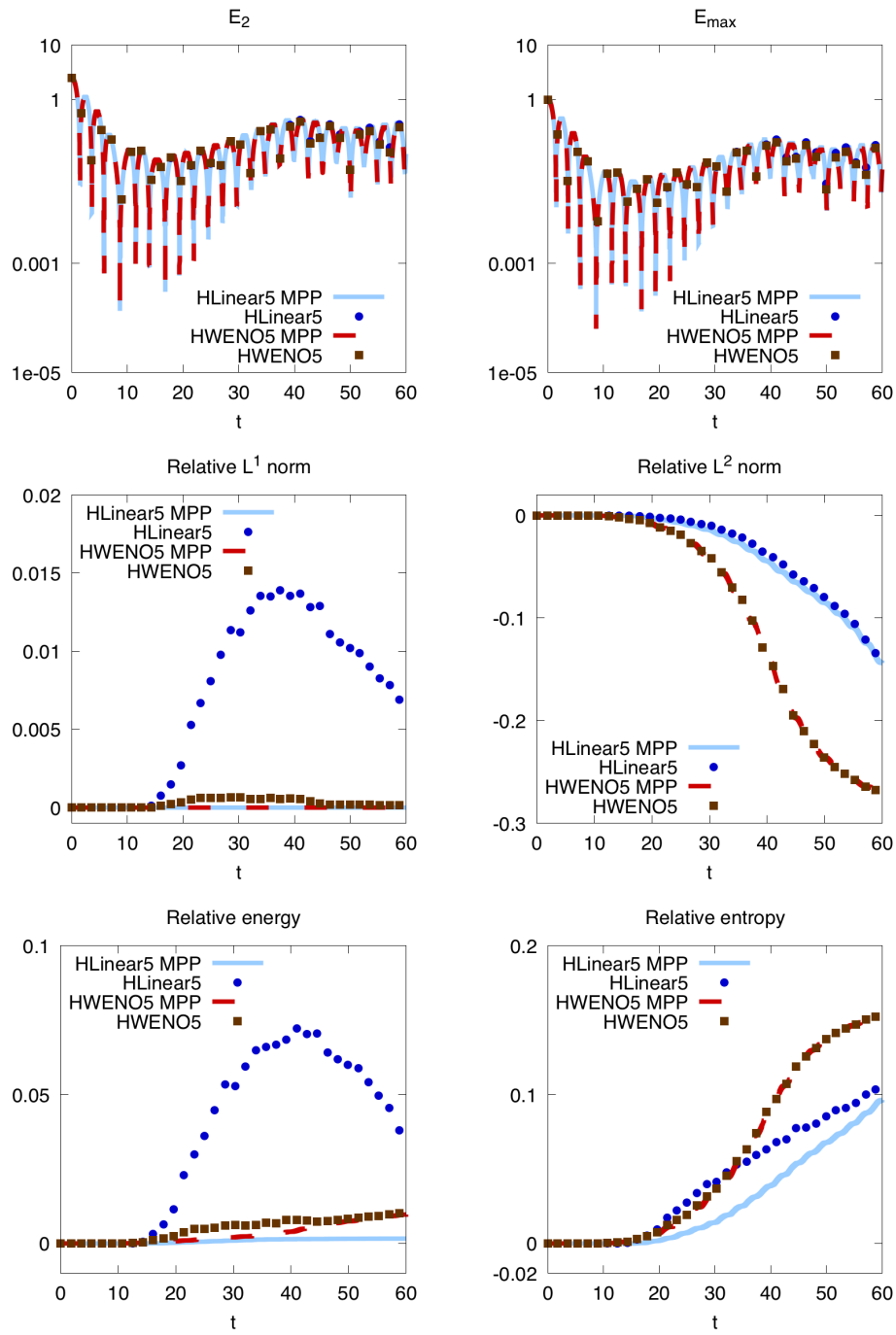


Figure 3: Strong Landau damping. Time evolution of the electric field in L^2 norm and L^∞ norm (top), relative differences of discrete L^1 norm and L^2 norm (middle), relative differences of kinetic energy and entropy (bottom). Mesh grid: 256×256 .

Especially for the energy, “HLinear5 MPP” is much better than all other schemes. This example has clearly show the good performance of our approach.

Example 3.4. (Symmetric two stream instability) We now consider the symmetric two stream instability with the initial condition:

$$f(0, x, v) = \frac{1}{2v_{th}\sqrt{2\pi}} \left[\exp\left(-\frac{(v-u)^2}{2v_{th}^2}\right) + \exp\left(-\frac{(v+u)^2}{2v_{th}^2}\right) \right] (1 + \alpha \cos(kx)), \quad (3.11)$$

where $\alpha = 0.05$, $u = 0.99$, $v_{th} = 0.3$ and $k = \frac{2}{13}$. Similarly, from the initial data, the minimum value of the solution is taking $v = 2\pi$ and $\cos(kx) = -1$ in (3.11), while the maximum value is taking $v = u$ or $v = -u$, and $\cos(kx) = 1$. We plot the numerical solution at $T = 70$ in Fig. 4 for the “HLinear5” and “HLinear5 MPP” schemes respectively. The mesh grid is 256×256 . We can also clearly observe that without limiter, the solution becomes negative, which, however, can be eliminated by the scheme with limiter. We show the time evolution of the electric field in L^2 norm and L^∞ norm, the relative derivation of the discrete L^1 norm, L^2 norm, kinetic energy and entropy in Fig. 5. Similar results as the last example are obtained.

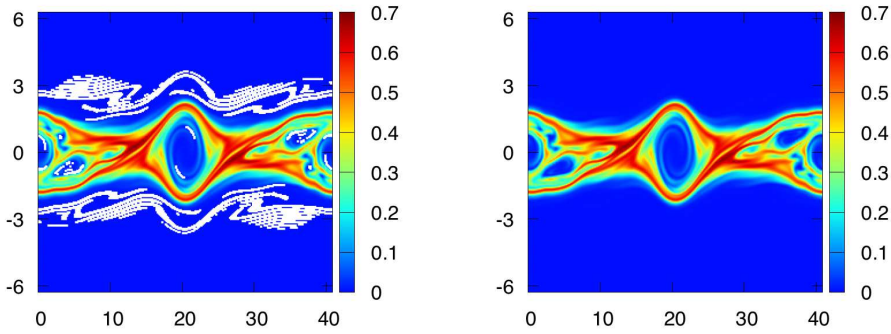


Figure 4: Symmetric two stream instability at $T = 70$. Left: without limiter; Right: with limiter. Mesh grid: 256×256 .

Example 3.5. (Bump-on-tail instability) We consider the bump-on-tail instability problem [2, 45] with the initial condition as

$$f(0, x, v) = f_{b.o.t}(v)(1 + \alpha \cos(kx)), \quad (3.12)$$

where the bump-on-tail distribution is

$$f_{b.o.t}(v) = \frac{n_p}{\sqrt{2\pi}} \exp\left(-\frac{v^2}{2}\right) + \frac{n_b}{\sqrt{2\pi}} \exp\left(-\frac{(v-v_b)^2}{2v_t^2}\right), \quad (3.13)$$

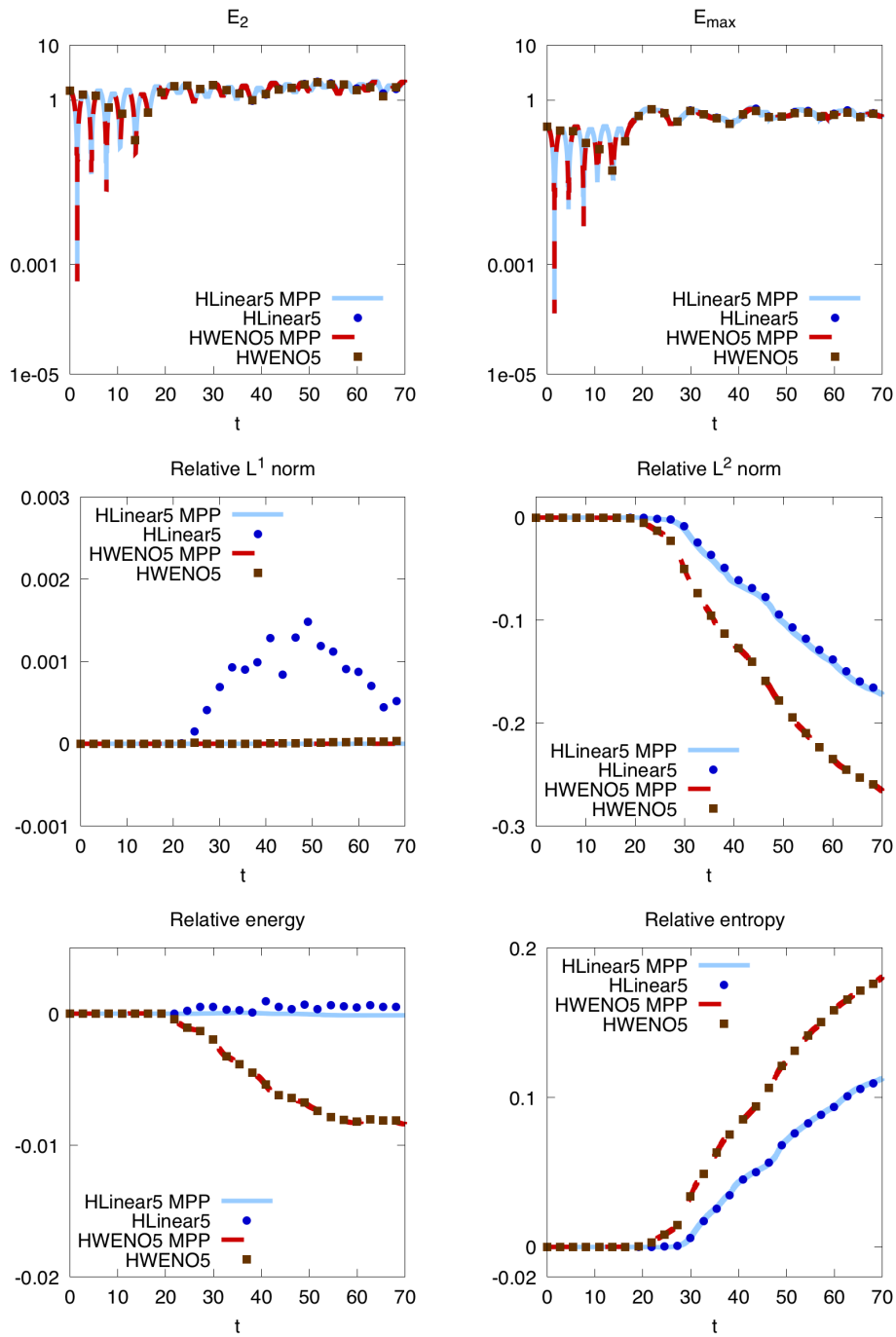


Figure 5: Symmetric two stream instability. Time evolution of the electric field in L^2 norm and L^∞ norm (top), relative differences of discrete L^1 norm and L^2 norm (middle), relative differences of kinetic energy and entropy (bottom). Mesh grid: 256×256 .

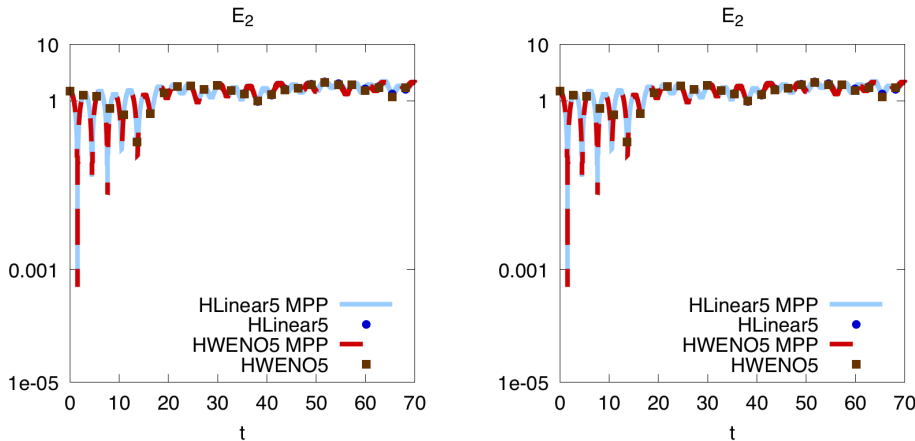


Figure 6: Bump-on-tail instability at $T=500$. Left: without limiter; Right: with limiter. Mesh grid: 256×256 .

and $n_p = 0.9$, $n_b = 0.2$, $v_b = 4.5$, $v_t = 0.5$, $\alpha = 0.04$, $k = 0.3$. The computational domain is $[0, \frac{2\pi}{k}] \times [-3\pi, 3\pi]$. We take the cut-off domain in v a little larger for the consideration of the shifting v_b in the velocity. For this problem, the minimum value of the initial data is taking $v = -3\pi$ and $\cos(kx) = -1$ in (3.12) and (3.13), while the maximum value is taking $v = 0$ and $\cos(kx) = 1$. We run a long time simulation up to $T = 1000$, which is a good test to show the effectiveness of the linear scheme in preserving some important quantities and the saving of computational cost as compared to the WENO type scheme. We first show the surface of the distribution function at $T = 500$ in Fig. 6. We can clearly observe without limiter, the solution has undershootings, while the scheme with limiter produces very good result. We show the time evolution of the electric field in L^2 norm and L^∞ norm in Fig. 7, and compare the linear scheme with the WENO type scheme. The L^∞ norm of the electric field E_{\max} matches those in [2, 45]. However, we can see that the linear scheme preserves the electric field better than the WENO type scheme after some large time, e.g., $T = 400$, while the results are almost the same between with and without limiter. We then show the relative derivation of the discrete L^1 norm, L^2 norm, kinetic energy and entropy in Fig. 8. The MPP limiter almost does not affect the L^2 norm and entropy, however, again we can see it improves the L^1 norm and the energy a lot from eliminating negative numerical values, which indicates the great performance of the MPP limiter on the linear scheme. Besides, the linear scheme preserves the L^2 norm, entropy and energy much better than the WENO type scheme, especially the energy.

We now take the Example 3.4 and Example 3.5 with long time simulations to compare the computational cost. We consider the ‘‘HLinear5 MPP’’ and ‘‘HWENO5 MPP’’ schemes. For Example 3.4, we run up to $T = 70$, while for Example 3.5 up to $T = 100$. The computational time for the linear type scheme is about $4m52s$ and $10m4s$ for the linear scheme, for two examples respectively. It is around $8m34s$ and $17m55s$ for the corresponding WENO type scheme. The linear scheme saves about 40% of the computational

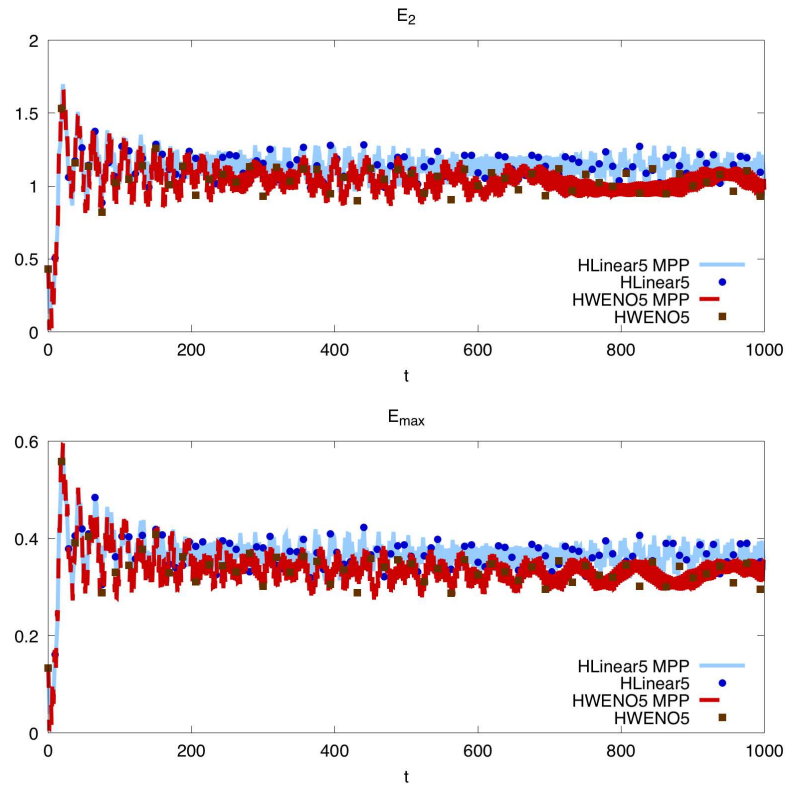


Figure 7: Bump-on-tail instability. Time evolution of the electric field in L^2 norm (top) and L^∞ norm (bottom). Mesh grid: 256×256 .

time than a WENO type scheme, which verifies the linear scheme is computational much more efficient.

3.3 Kelvin-Helmholtz instability

Example 3.6. The Kelvin-Helmholtz instability comes from the 2D guiding-center model (1.4) [21] with the initial data

$$\rho_0(x, y) = \sin(y) + 0.015 \cos(kx) \quad (3.14)$$

and periodic boundary conditions on the domain $[0, 4\pi] \times [0, 2\pi]$. We let $k = 0.5$, which will create a Kelvin-Helmholtz instability. The exact solution should be within the range $[-1.015, 1.015]$.

For this example, we show the solution at $T = 40$ with mesh grid 256×256 for “HLinear5” and “HLinear5 MPP” in Fig. 9 respectively. For the figures drawing in the physical range $[-1.015, 1.015]$, we can observe white spots for “HLinear5” which is without MPP limiter, while “HLinear5 MPP” with MPP limiter preserves the bounds very well. In

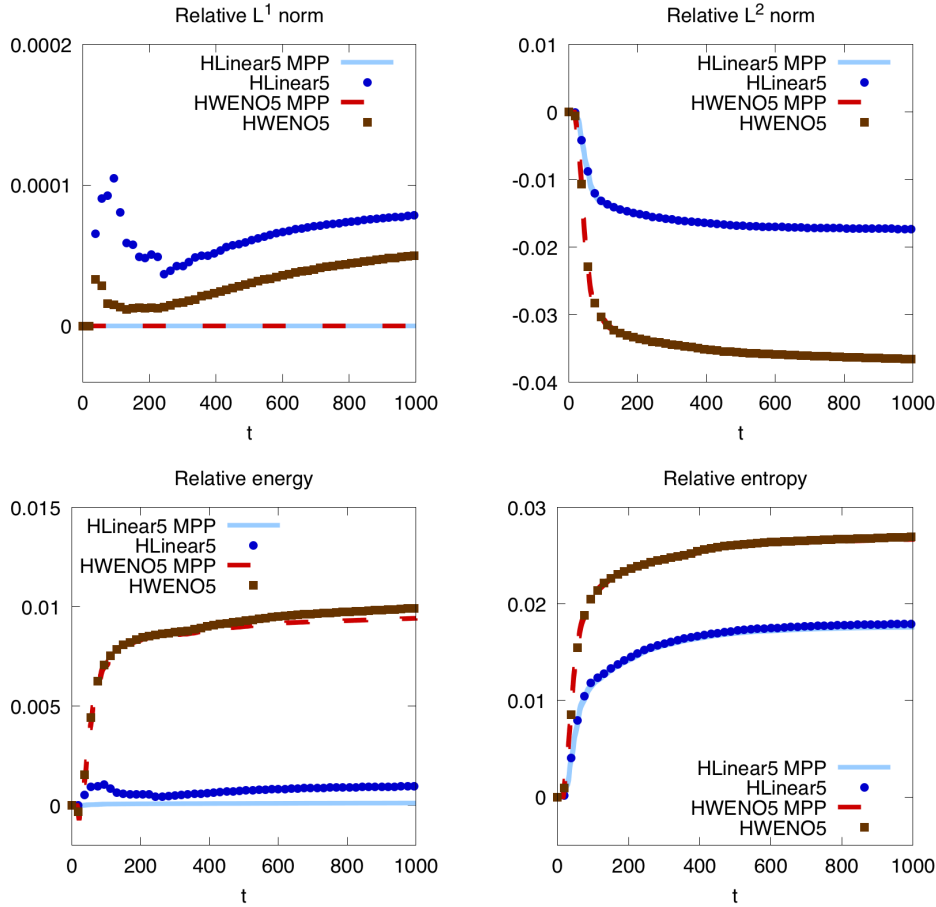


Figure 8: Bump-on-tail instability. Time evolution of the relative differences of discrete L^1 norm and L^2 norm (top), relative differences of kinetic energy and entropy (bottom). Mesh grid: 256×256 .

Fig. 10, we compare the time evolution of the relative L^2 norm and the numerical minimum values for both linear and WENO type schemes without and with limiters respectively. First, we can find that the linear scheme is less dissipative than the WENO one, as the L^2 norm preserves better for the linear scheme. The schemes with and without MPP limiter preserves the L^2 norm almost the same, so that there is no significant affection from the MPP limiter. For the minimum numerical values, the linear scheme without MPP limiter has shown large undershootings, the WENO type scheme without MPP limiter performs even worse for this example (with the same time step as the linear scheme), but both schemes with MPP limiter preserve the lower bound very well. Similarly for the upper bound.

From this example, we can see that for problems with highly oscillatory but without discontinuous solutions, a high order linear scheme with the MPP limiter can result in a

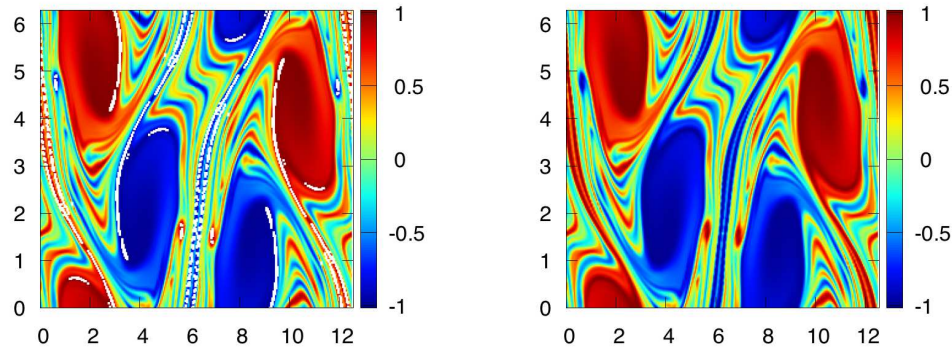


Figure 9: Kelvin-Helmholtz instability problem at $T = 40$. Mesh grid: 256×256 . Left: "HLinear5"; Right: "HLinear5 MPP".

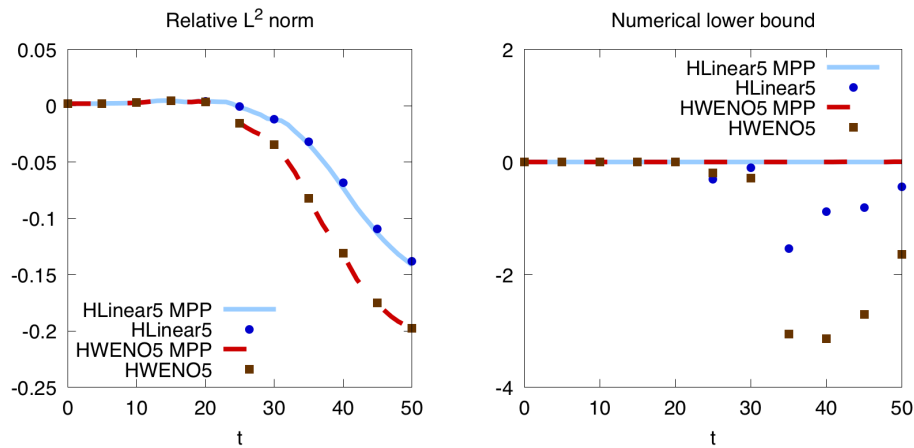


Figure 10: Kelvin-Helmholtz instability problem. Mesh grid: 256×256 . Left: relative L^2 norm; right: numerical minimum bound ($\rho_m + 1.015$).

very good scheme, which is less dissipative and without significant spurious oscillations. The original idea to apply WENO reconstruction to suppress numerical oscillations may require smaller time steps when the solution evolves finer and finer. We can take this example as a benchmark test to support our main idea in this paper.

3.4 Incompressible Euler equations

Example 3.7. (Accuracy test) We first consider the incompressible Euler system on the domain $[0, 2\pi] \times [0, 2\pi]$ with an initial condition $\omega_0(x, y) = -2\sin(x)\sin(y)$. The exact solution will stay stationary with $\omega(x, y, t) = -2\sin(x)\sin(y)$, which is in the range of $[-2, 2]$.

Table 4: Example 3.7. ω_{\min} and ω_{\max} are the minimum and maximum numerical solutions respectively. "WO" stands for "without limiter", "WL" stands for "with limiter". $T=1$.

	N	L^1 error	order	L^∞ error	order	ω_{\max}	ω_{\min}
WO	32	2.34e-05	–	4.89e-05	–	2	-2
	64	8.86e-07	4.72	1.63e-06	4.91	2	-2
	128	2.93e-08	4.92	5.08e-08	5.00	2	-2
	256	9.43e-10	4.96	1.60e-09	4.99	2	-2
WL	32	2.34e-05	–	4.89e-05	–	2	-2
	64	8.86e-07	4.72	1.63e-06	4.91	2	-2
	128	2.93e-08	4.92	5.08e-08	5.00	2	-2
	256	9.43e-10	4.96	1.60e-09	4.99	2	-2

For this example, from Table 4, we can see that the numerical solution with and without the limiter all stay in the right range, which shows that the limiter does not destroy the high order accuracy.

Example 3.8. (Vortex patch). In this example, we consider the incompressible Euler equations for the vortex patch problem with the initial condition given by

$$\omega_0(x,y) = \begin{cases} -1, & \frac{\pi}{2} \leq x \leq \frac{3\pi}{2}, \frac{\pi}{4} \leq y \leq \frac{3\pi}{4}; \\ 1, & \frac{\pi}{2} \leq x \leq \frac{3\pi}{2}, \frac{5\pi}{4} \leq y \leq \frac{7\pi}{4}; \\ 0, & \text{otherwise.} \end{cases} \quad (3.15)$$

We show the surface of ω at $T=10$ in Fig. 11. The mesh grid is 256×256 . We can observe the good performance of the MPP flux limiter on this problem. We also show the time evolution of the relative difference of L^2 norm as compared to the initial data, and the minimum numerical solution on the bottom of Fig. 11. Here we can still see that the linear scheme preserves the L^2 norm better than the WENO type scheme and the MPP limiter can eliminate the oscillations around two extreme values 1 and -1 from the schemes without limiter. However, we would mention that for this example with discontinuous initial data, the MPP limiter cannot remove the small numerical oscillations around 0 (figures are omitted here). In this case, the WENO will be needed to completely remove oscillations for middle discontinuities.

4 Conclusion

In this paper, we have proposed a linear scheme combined with a high order bound-preserving MPP flux limiter, for solving incompressible flow problems. As compared

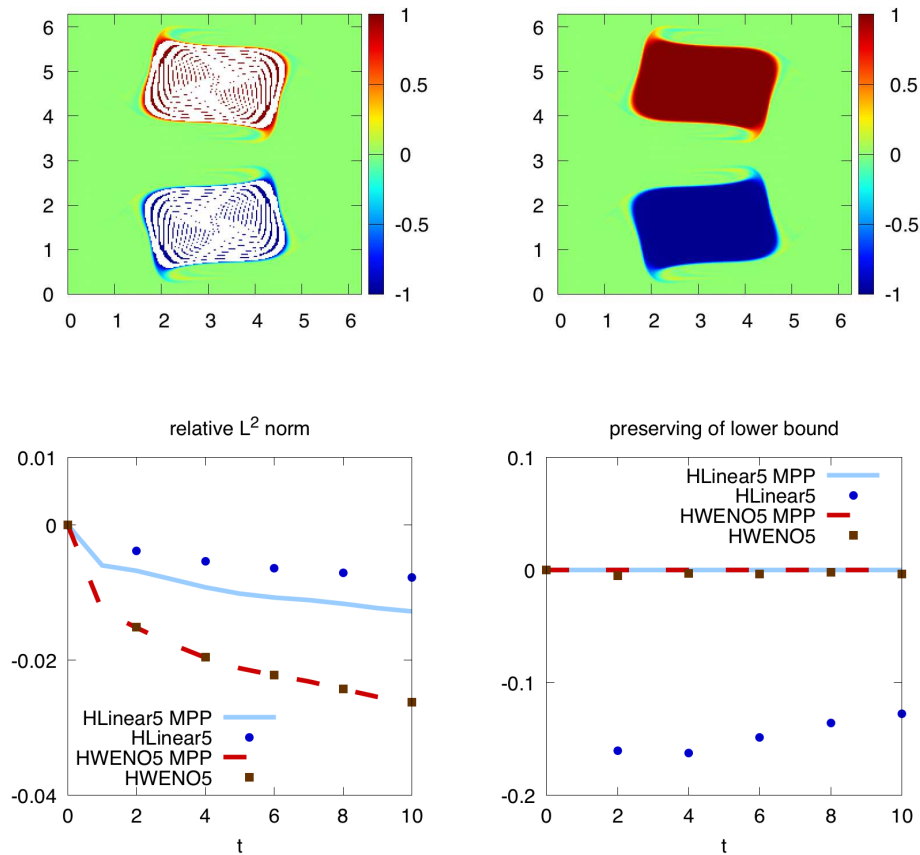


Figure 11: The vortex patch problem. Mesh grid: 256×256 . Top: surface of the vorticity ω at $T=10$ without and with MPP limiter on the left and right respectively. Bottom: the relative L^2 norm and the numerical minimum bound ($\omega_m + 1$).

to WENO type schemes, our approach is less dissipative and much less costly, so that is much more efficient for high dimensional problems with long time simulations. Applications to the Vlasov-Poisson system, 2D guiding-center model in plasma physics, as well as the incompressible Euler equations in fluid hydrodynamics have demonstrated the good performance of our proposed approach.

Acknowledgments

T. Xiong acknowledges support by NSFC grant No. 11971025, NSF grant of Fujian Province No. 2019J06002, the Strategic Priority Research Program of Chinese Academy of Sciences Grant No. XDA25010401.

References

- [1] S. Abarbanel, D. Gottlieb and M. H. Carpenter, On the removal of boundary errors caused by Runge-Kutta time integration of nonlinear partial differential equations, *SIAM J. Sci. Comput.*, 17 (1996), 777-782.
- [2] T. Arber and R. Vann, A critical comparison of Eulerian-grid-based Vlasov solvers, *J. Comput. Phys.*, 180 (2002), 339-357.
- [3] C.-W. Shu, J. A. Carrillo and B. Ayuso, Discontinuous Galerkin methods for the one-dimensional Vlasov-Poisson system, *Kinet. Real. Mod.*, 4 (2013), 955-989.
- [4] N. Besse, E. Deriaz and É. Madaule, Adaptive multiresolution semi-Lagrangian discontinuous Galerkin methods for the Vlasov equations, *J. Comput. Phys.*, 332 (2017), 376-417.
- [5] N. Besse and E. Sonnendrücker, Semi-Lagrangian schemes for the Vlasov equation on an unstructured mesh of phase space, *J. Comput. Phys.*, 191 (2003), 341-376.
- [6] X. Cai, S. Boscarino and J.-M. Qiu, High order semi-Lagrangian discontinuous Galerkin method coupled with Runge-Kutta exponential integrator for nonlinear Vlasov dynamics, *J. Comput. Phys.*, 427 (2021), 110036.
- [7] X. Cai, W. Guo and J.-M. Qiu, Comparison of semi-Lagrangian discontinuous Galerkin schemes for linear and nonlinear transport simulations, *Commun. Appl. Math. Comput.*, 4 (2022), 3-33.
- [8] X. Cai, J. Qiu and J.-M. Qiu, A conservative semi-Lagrangian HWENO method for the Vlasov equation, *J. Comput. Phys.*, 323 (2016), 95-114.
- [9] M. H. Carpenter, D. Gottlieb, S. Abarbanel and W.-S. Don, The theoretical accuracy of Runge-Kutta time discretizations for the initial boundary value problem: a study of the boundary error, *SIAM J. Sci. Comput.*, 16 (1995), 1241-1252.
- [10] J. A. Carrillo and F. Vecil, Nonoscillatory interpolation methods applied to Vlasov-based models, *SIAM J. Sci. Comput.*, 29 (2007), 1179-1206.
- [11] Y. Cheng, I. M. Gamba and P. J. Morrison, Study of conservation and recurrence of Runge-Kutta discontinuous Galerkin schemes for Vlasov-Poisson systems, *J. Sci. Comput.*, 56 (2013), 319-349.
- [12] A. Christlieb, W. Guo and Y. Jiang, A WENO-based method of lines transpose approach for Vlasov simulations, *J. Comput. Phys.*, 327 (2016), 337-367.
- [13] N. Crouseilles, M. Mehrenberger and E. Sonnendrücker, Conservative semi-Lagrangian schemes for Vlasov equations, *J. Comput. Phys.*, 229 (2010), 1927-1953.
- [14] N. Crouseilles, M. Mehrenberger and F. Vecil, Discontinuous Galerkin semi-Lagrangian method for Vlasov-Poisson, in *ESAIM: Proceedings, EDP Sciences*, 32 (2011), 211-230.
- [15] B. A. Dios, J. A. Carrillo and C.-W. Shu, Discontinuous Galerkin methods for the multi-dimensional Vlasov-Poisson problem, *Math. Models. Methods. Appl. Sci.*, 22 (2012), 195-283.
- [16] W.-S. Don, Z. Gao, P. Li and X. Wen, Hybrid compact-WENO finite difference scheme with conjugate Fourier shock detection algorithm for hyperbolic conservation laws, *SIAM J. Sci. Comput.*, 38 (2016), A691-A711.
- [17] Q. Dong, S. Su and J. Wu, A decoupled and positivity-preserving ddfvs scheme for diffusion problems on polyhedral meshes, *Commun. Comput. Phys.*, 27 (2020), 1378-1412.
- [18] E. Fijalkow, A numerical solution to the Vlasov equation, *Comput. Phys. Commun.*, 116 (1999), 319-328.
- [19] F. Filbet and E. Sonnendrücker, Comparison of Eulerian Vlasov solvers, *Comput. Phys. Commun.*, 150 (2003), 247-266.

- [20] F. Filbet, E. Sonnendrücker and P. Bertrand, Conservative numerical schemes for the Vlasov equation, *J. Comput. Phys.*, 172 (2001), 166-187.
- [21] E. Frénod, S. A. Hirstoaga, M. Lutz and E. Sonnendrücker, Long time behaviour of an exponential integrator for a Vlasov-Poisson system with strong magnetic field, *Commun. Comput. Phys.*, 18 (2015), 263-296.
- [22] W. Guo and Y. Cheng, An adaptive multiresolution discontinuous Galerkin method for time-dependent transport equations in multidimensions, *SIAM J. Sci. Comput.*, 39 (2017), A2962-A2992.
- [23] W. Guo and J.-M. Qiu, Hybrid semi-Lagrangian finite element-finite difference methods for the Vlasov equation, *J. Comput. Phys.*, 234 (2013), 108-132.
- [24] R. E. Heath, I. M. Gamba, P. J. Morrison and C. Michler, A discontinuous Galerkin method for the Vlasov-Poisson system, *J. Comput. Phys.*, 231 (2012), 1140-1174.
- [25] F. Jia, Z. Gao and W. S. Don, A spectral study on the dissipation and dispersion of the WENO schemes, *J. Sci. Comput.*, 63 (2015), 49-77.
- [26] C. Liang and Z. Xu, Parametrized maximum principle preserving flux limiters for high order schemes solving multi-dimensional scalar hyperbolic conservation laws, *J. Sci. Comput.*, 58 (2014), 41-60.
- [27] M. Liu, S. Shu, G. Yuan and X. Yue, Two nonlinear positivity-preserving finite volume schemes for three-dimensional heat conduction equations on general polyhedral meshes, *Commun. Comput. Phys.*, 30 (2021), 1185-1215.
- [28] E. Madaule, S. A. Hirstoaga, M. Mehrenberger and J. Pétri, Semi-Lagrangian simulations of the diocotron instability, *Research Report*, hal-00841504, (2013).
- [29] É. Madaule, M. Restelli and E. Sonnendrücker, Energy conserving discontinuous Galerkin spectral element method for the Vlasov-Poisson system, *J. Comput. Phys.*, 279 (2014), 261-288.
- [30] D. Pathria, The correct formulation of intermediate boundary conditions for Runge-Kutta time integration of initial boundary value problems, *SIAM J. Sci. Comput.*, 18 (1997), 1255-1266.
- [31] J.-M. Qiu and A. Christlieb, A conservative high order semi-Lagrangian WENO method for the Vlasov equation, *J. Comput. Phys.*, 229 (2010), 1130-1149.
- [32] J.-M. Qiu and G. Russo, A high order multi-Dimensional characteristic tracing strategy for the Vlasov-Poisson system, *J. Sci. Comput.*, 71 (2017), 414-434.
- [33] J.-M. Qiu and C.-W. Shu, Conservative semi-Lagrangian finite difference WENO formulations with applications to the Vlasov equation, *Commun. Comput. Phys.*, 10 (2011), 979-1000.
- [34] J.-M. Qiu and C.-W. Shu, Positivity preserving semi-Lagrangian discontinuous Galerkin formulation: theoretical analysis and application to the Vlasov-Poisson system, *J. Comput. Phys.*, 230 (2011), 8386-8409.
- [35] J. A. Rossmannith and D. C. Seal, A positivity-preserving high-order semi-Lagrangian discontinuous Galerkin scheme for the Vlasov-Poisson equations, *J. Comput. Phys.*, 230 (2011), 6203-6232.
- [36] C.-W. Shu, Essentially non-oscillatory and weighted essentially non-oscillatory schemes for hyperbolic conservation laws, in *Advanced Numerical Approximation of Nonlinear Hyperbolic Equations*, Springer, 1998, 325-432.
- [37] C.-W. Shu and S. Osher, Efficient implementation of essentially non-oscillatory shock-capturing schemes, *J. Comput. Phys.*, 77 (1988), 439-471.
- [38] E. Sonnendrücker, J. Roche, P. Bertrand and A. Ghizzo, The semi-Lagrangian method for the

- numerical resolution of the Vlasov equation, *J. Comput. Phys.*, 149 (1999), 201-220.
- [39] S. Su, H. Tang and J. Wu, An efficient positivity-preserving finite volume scheme for the nonequilibrium three-temperature radiation diffusion equations on polygonal meshes, *Commun. Comput. Phys.*, 30 (2021), 448-485.
- [40] S. Su and J. Wu, A vertex-centered and positivity-preserving finite volume scheme for two-dimensional three-temperature radiation diffusion equations on general polygonal meshes, *Numer. Math-Theory. Me.*, 13 (2020), 220-252.
- [41] S. Tan and C.-W. Shu, Inverse Lax-Wendroff procedure for numerical boundary conditions of conservation laws, *J. Comput. Phys.*, 229 (2010), 8144-8166.
- [42] S. Tan, C. Wang, C.-W. Shu and J. Ning, Efficient implementation of high order inverse Lax-Wendroff boundary treatment for conservation laws, *J. Comput. Phys.*, 231 (2012), 2510-2527.
- [43] T. Xiong, J.-M. Qiu and Z. Xu, A parametrized maximum principle preserving flux limiter for finite difference RK-WENO schemes with applications in incompressible flows, *J. Comput. Phys.*, 252 (2013), 310-331.
- [44] T. Xiong, J.-M. Qiu and Z. Xu, Parametrized positivity preserving flux limiters for the high order finite difference WENO scheme solving compressible Euler equations, *J. Sci. Comput.*, 67 (2016), 1066-1088.
- [45] T. Xiong, J.-M. Qiu, Z. Xu and A. Christlieb, High order maximum principle preserving semi-Lagrangian finite difference WENO schemes for the Vlasov equation, *J. Comput. Phys.*, 273 (2014), 618-639.
- [46] T. Xiong, G. Russo and J.-M. Qiu, Conservative multi-dimensional semi-Lagrangian finite difference scheme: stability and applications to the kinetic and fluid simulations, *J. Sci. Comput.*, 79 (2019), 1241-1270.
- [47] T. Xiong, M. Zhang, Y.-T. Zhang and C.-W. Shu, Fast sweeping fifth order WENO scheme for static Hamilton-Jacobi equations with accurate boundary treatment, *J. Sci. Comput.*, 45 (2010), 514-536.
- [48] J. Xu, F. Zhao, Z. Sheng and G. Yuan, A nonlinear finite volume scheme preserving maximum principle for diffusion equations, *Commun. Comput. Phys.*, 29 (2021), 747-766.
- [49] Z. Xu, Parametrized maximum principle preserving flux limiters for high order schemes solving hyperbolic conservation laws: one-dimensional scalar problem, *Math. Comput.*, 83 (2014), 2213-2238.
- [50] Z. Xu and X. Zhang, Bound-preserving high-order schemes, in *Handbook of Numerical Analysis*, 18 (2017), 81-102.
- [51] C. Yang and F. Filbet, Conservative and non-conservative methods based on Hermite weighted essentially non-oscillatory reconstruction for Vlasov equations, *J. Comput. Phys.*, 279 (2014), 18-36.
- [52] C. Yang and M. Mehrenberger, Highly accurate monotonicity-preserving Semi-Lagrangian scheme for Vlasov-Poisson simulations, *J. Comput. Phys.*, 446 (2021), 110632.
- [53] S. Zaki, T. Boyd and L. Gardner, A finite element code for the simulation of one-dimensional Vlasov plasmas. II. Applications, *J. Comput. Phys.*, 79 (1988), 200-208.
- [54] S. Zaki, L. Gardner and T. Boyd, A finite element code for the simulation of one-dimensional Vlasov plasmas. I. theory, *J. Comput. Phys.*, 79 (1988), 184-199.
- [55] M. Zhang, W. Huang and J. Qiu, A well-balanced positivity-preserving quasi-Lagrange moving mesh DG method for the shallow water equations, *Commun. Comput. Phys.*, 31 (2022), 94-130.
- [56] X. Zhang, Y. Xia and C.-W. Shu, Maximum-principle-satisfying and positivity-preserving

- high order discontinuous Galerkin schemes for conservation laws on triangular meshes, *J. Sci. Comput.*, 50 (2012), 29-62.
- [57] W. Zhao, J. Huang and S. J. Ruuth, Boundary treatment of high order Runge-Kutta methods for hyperbolic conservation laws, *J. Comput. Phys.*, 421 (2020), 109697.
- [58] N. Zheng, X. Cai, J.-M. Qiu and J. Qiu, A conservative semi-Lagrangian hybrid Hermite WENO scheme for linear transport equations and the nonlinear Vlasov-Poisson system, *SIAM J. Sci. Comput.*, 43 (2021), A3580-A3606.
- [59] T. Zhou, Y. Guo and C.-W. Shu, Numerical study on Landau damping, *Physica. D.*, 157 (2001), 322-333.
- [60] H. Zhu, J. Qiu and J.-M. Qiu, An h-Adaptive RKDG method for the Vlasov-Poisson system, *J. Sci. Comput.*, 69 (2016), 1346-1365.